RSC Advances

PAPER

View Article Online
View Journal | View Issue

Cite this: *RSC Adv.*, 2021, **11**, 4864

Controllable preparation of one-dimensional $Li_{1.2}Mn_{0.54}Ni_{0.13}Co_{0.13}O_2$ cathode materials for high-performance lithium-ion batteries

Zhi Gao,[a] Jiayi Zhao,[a] Xiaoliang Pan,*[a] Lijun Liu,[b] Shikun Xie[a] and Huiling Yuan[a]

Received 21st November 2020
Accepted 20th January 2021

DOI: 10.1039/d0ra09880a

rsc.li/rsc-advances

Lithium-rich layered oxides are attractive candidates of high-energy-density cathode materials for high-performance lithium ion batteries because of their high specific capacity and low cost. Nevertheless, their unsatisfactory rate capability and poor cycling stability have strongly hindered commercial applications in lithium ion batteries, mainly due to the ineffectiveness of the complicated synthesis techniques to control their morphologies and sizes. In this work, the $Li_{1.2}Mn_{0.54}Ni_{0.13}Co_{0.13}O_2$ cathode materials with a one-dimensional rod-like morphology were synthesized *via* a facile co-precipitation route followed by a post-calcination treatment. By reasonably adding $NH_3 \cdot H_2O$ in the co-precipitation reaction, the sizes of the metal oxalate precursors could be rationally varied. The electrochemical measurements displayed that the $Li_{1.2}Mn_{0.54}Ni_{0.13}Co_{0.13}O_2$ short rods delivered a high capacity of 286 mA h g^{-1} at 0.1C and excellent capacity retention of 85% after 100 cycles, which could be contributed to the improvement of the electrolyte contact, Li^+ diffusion, and structural stability of the one-dimension porous structure.

1. Introduction

The energy and power densities of lithium-ion batteries strongly depend on the properties of cathode materials.[1,2] Developing cathode materials with large reversible capacities, high rate capabilities and good cycling stabilities are of great importance for the improvements of electrochemical properties of the whole cells.[3,4] Among cathode materials explored so far, lithium-rich layered oxides, $xLi_2MnO_3\,(1-x)LiMO_2$ ($0 < x < 1$; M = Mn, Ni or/and Co), have been considered as some of the most promising cathode materials to meet the requirements for high energy densities of lithium-ion batteries owing to their high reversible capacity (>250 mA h g^{-1}) and high working voltage (>3.5 V *vs.* Li/Li^+), as well as low cost.[5–7] However, there are still some serious problems preventing large scale commercial applications of lithium-rich layered oxides, such as the unsatisfactory rate capability, the poor cycling stability and the rapid decay of average voltage upon repeated cycling.[8–10]

Recently, cathode materials with a one-dimensional morphology have attracted intensive research interest for their enhanced electrochemical performance due to the short diffusion path, the high specific surface area, and the ability to ease the strain caused by the repeated insertion/extraction of lithium ions.[11–13] Thus, much work has been devoted on the syntheses of lithium-rich layered oxides with a typical one-dimensional morphology to improve their electrochemical performance. For examples, the bars were prepared by a co-precipitation method and the following calcination process, and the aspect ratios of the bars were controlled by tuning the ethanol–water volume ratio, and $0.5Li_2MnO_3 \cdot 0.5LiNi_{1/3}Co_{1/3}Mn_{1/3}O_2$ bars demonstrated the excellent capacity and rate capability;[14] $Li_{1.2}Ni_{0.13}Co_{0.13}Mn_{0.54}O_2$ with rod-like, olive-like and shuttle-like morphologies were fabricated by the co-precipitation route followed by subsequent annealing treatment process, and the morphologies of the products were tailored by controlling the volume ratio of ethylene glycol with the assistance of surfactant, and the olives achieved better electrochemical performance;[15] $Li_{1.2}Ni_{0.15}Co_{0.1}Mn_{0.55}O_2$ cross-linked nanorods and agglomerate microrods were synthesized *via* using carbon-decorated MnO_2 nanowires and MnO_2 nanorods as templates, and the cross-linked nanorods exhibited superior discharge capacity and cycling stability.[16]

From above-mentioned literatures, the manipulations of the one-dimensional morphology for lithium-rich layered oxides have been proved as an accessible approach in modulating their electrochemical properties. Meanwhile, it is clear that the further exploration to optimize the morphology and size for lithium-rich layered oxides is of tremendous significance in improvements of their electrochemical properties. To date, limited success has been achieved for a simply size-controlled synthesis of lithium-rich layered oxides with the one-dimensional morphology.

[a]School of Mechanical Engineering, Jinggangshan University, Jian, 343009, China. E-mail: xiaoliang_pan@163.com

[b]School of Chemistry and Chemical Engineering, Jinggangshan University, Jian, 343009, China

Herein, we report a simple strategy to fabricate the $Li_{1.2}Mn_{0.54}Ni_{0.13}Co_{0.13}O_2$ rods with controllable sizes. The whole strategy mainly consists of two steps. For the first step, the metal oxalate precursors are synthesized by a co-precipitation method at room temperature. Importantly, the size of the precursors can be tuned by simply adding $NH_3 \cdot H_2O$ in the co-precipitation reaction. For the second step, the metal oxalate precursors are calcined in air, obtaining the final $Li_{1.2}Mn_{0.54}Ni_{0.13}Co_{0.13}O_2$ rods. The effects of the size on the electrochemical performance of the as-prepared cathode materials are systematically investigated. This work provides a simple strategy for the design and control of the one-dimensional morphology and size for lithium-rich layered oxides using in lithium-ion batteries.

2. Experimental

2.1. Materials syntheses

The $Li_{1.2}Mn_{0.54}Ni_{0.13}Co_{0.13}O_2$ cathode materials with the one-dimensional morphology were fabricated by a facile co-precipitation method followed by a post-calcination treatment. In a typical synthesis, 8.4 mmol lithium acetate ($LiCH_3COO \cdot 2H_2O$), 3.6 mmol manganese acetate ($Mn(CH_3COO)_2 \cdot 4H_2O$), 0.87 mmol nickel acetate ($Ni(CH_3COO)_2 \cdot 4H_2O$) and 0.87 mmol cobalt acetate ($Co(CH_3COO)_2 \cdot 4H_2O$) were sufficiently dissolved in the mixture of 30 ml ethanol and 5 ml $NH_3 \cdot H_2O$ at room temperature, while 19.08 mmol oxalate ($H_2C_2O_4 \cdot 2H_2O$) was dissolved into another 10 ml ethanol. Then, the oxalic acid solution was rapidly poured into the mixed metal-acetate solution under stirring for 4 h to form the pink precipitate which was subsequently dried at 80 °C overnight to obtain the metal oxalate precursor. Finally, the metal oxalate precursor was calcined at 450 °C for 5 h, 750 °C for 10 h in air at a heating rate of 3.5 °C min^{-1} and then quenched naturally in the furnace to obtain the $Li_{1.2}Mn_{0.54}Ni_{0.13}Co_{0.13}O_2$ short rods. For comparison, the $Li_{1.2}Mn_{0.54}Ni_{0.13}Co_{0.13}O_2$ long rods were fabricated without $NH_3 \cdot H_2O$, while other conditions were kept unchanged.

2.2. Materials characterizations

The X-ray diffraction (XRD) patterns were recorded by an X-ray powder diffractometer (Rigaku D/max-rA diffractometer, Cu Kα radiation, $\lambda = 1.5406$ Å). The XRD refinements were conducted by Rietveld method with FullProf_suite program. The chemical compositions of the samples were analyzed by inductively coupled plasma-optical emission spectroscopy (ICP-OES, Agilent 730). The morphologies and structures of the samples were examined by a field-emission electron microscope (FE-SEM, FEI Quanta 200F), and a transmission electron microscope (JEOL, JEM-2100) with a high-resolution transmission electron microscopy. The specific surface areas of the samples were determined by the Brunauer–Emmett–Teller (BET) method (Micromeritics ASAP, 2020 M) with nitrogen as adsorption–desorption gas.

2.3. Electrochemical measurements

The electrochemical measurements were carried out using CR2032-type coin cells on a Land-CT2001A battery test system (Jinnuo Wuhan Corp.). All the tests were performed at room temperature.

The CR2032-type coin cells were assembled in an argon-filled glovebox using a metallic lithium foil as the anode, 1 M $LiPF_6$ in a 1 : 1 (in volume) mixture of ethylene carbonate (EC) and dimethyl carbonate (DMC) as the electrolyze, and Celgard 2400 polypropylene as the separator. Cathodes were fabricated by spreading a mixture of 80 wt% active material, 10 wt% acetylene black and 10 wt% polyvinylidene fluoride (PVDF) on an Al foil. Galvanostatic charge/discharge tests were carried out at different rates between 2.0 and 4.8 V (1C = 250 mA g^{-1}). Cyclic voltammetry (CV) measurements were recorded on a CHI660E electrochemical workstation (Chenhua Instruments Shanghai Inc.). Electrochemical impedance spectroscopy (EIS) tests were also recorded on the CHI660E electrochemical workstation, and an AC voltage signal of 5 mV was used over a frequency range from 0.01 to 100 000 Hz.

3. Results and discussion

3.1. Characterizations of the rods

Fig. 1 shows the XRD patterns of the metal oxalate precursors and the $Li_{1.2}Mn_{0.54}Ni_{0.13}Co_{0.13}O_2$ materials as well as the nitrogen adsorption–desorption isotherms. In Fig. 1a, the main diffraction peaks of the metal oxalate precursors are indexed to $Li_2C_2O_4$ (JCPDS no. 24-0646), $MnC_2O_4 \cdot 2H_2O$ (JCPDS no. 25-0544), $NiC_2O_4 \cdot 2H_2O$ (JCPDS no. 01-0299), and $CoC_2O_4 \cdot 2H_2O$ (JCPDS no. 25-0250) phases. In Fig. 1b, all of the XRD diffraction peaks are well indexed to a hexagonal α-$NaFeO_2$ structure with a space group of $R\bar{3}m$ where the Na-sites are occupied by Li while the Fe-sites are occupied by Mn, Ni, Co, and Li.[17,18] Notably, the sharp diffraction peaks imply the high crystallinity and no impurity peaks is detected, denoting the high purity of the final lithium-rich materials. Meanwhile, there are a few weak peaks detected around 20–25°, which are caused by the arrangement of Li^+ and Mn^{4+} in the transition metal layers of Li_2MnO_3 phase with $C2/m$ monoclinic symmetry.[19] Generally, the intensity ratio of (003) and (104) peaks corresponds to the degree of the Li^+/Ni^{2+} cation disordering in the lithium layers owing to their similar ion radii, and an over 1.2 of the ratio represents a negligible degree of the cation disordering.[20] The values of 1.8 and 1.7 for the short and long rods illustrate a low level of the cation disordering in their crystal lattices, respectively. Besides, the clear divisions of (006)/(012) and (108)/(110) doublets indicate their well-defined layered structure.[21,22]

To obtain the details of the structural differences, the XRD patterns of the two samples are analyzed by Rietveld refinement on the basis of $R\bar{3}m$ structure, as shown in Fig. 1c and d. The observed intensities are shown by the crosses, while the calculated patterns are shown by the solid lines. Bragg peak positions of $R\bar{3}m$ (JCPDS no. 09-0063) and $C2/m$ (JCPDS No. 84-1634) are shown by the vertical light and dark green bars, respectively. The corresponding lattice constants are tabulated in Table 1.

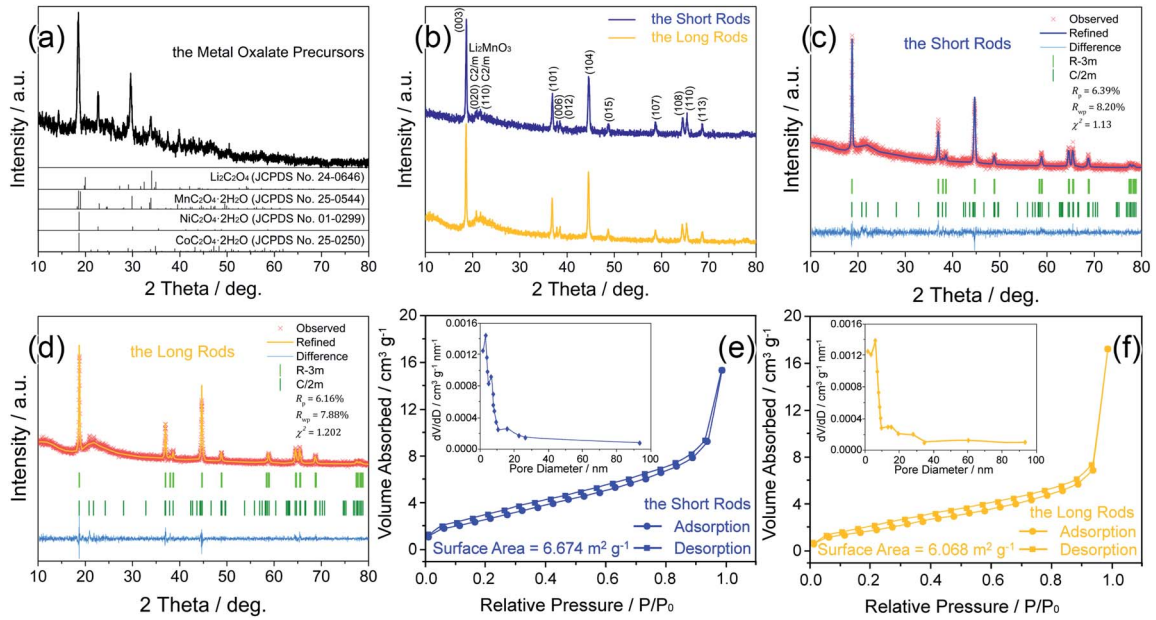

Fig. 1 XRD patterns (a and b) of the metal oxalate precursors and the $Li_{1.2}Mn_{0.54}Ni_{0.13}Co_{0.13}O_2$ rods, the Rietveld refinement results (c and d) and the nitrogen adsorption–desorption isotherms (e and f, the insets are the pore-size distribution plots).

Table 1 The Rietveld refinement data obtained from XRD

	Lattice constants/Å			Peak positions/deg.		
Sample	*a*	*c*	*c*/*a*	(003)	(104)	$I_{(003)}/I_{(104)}$
The short rods	2.851	14.217	4.987	18.676	44.645	1.812
The long rods	2.850	14.195	4.981	18.632	44.526	1.746

According to the refinement results, there are slight differences in lattice constants for the two samples. Their size ratios of *c*/*a* are larger than that of idea cubic close stacking (the ratio is 4.899), confirming both of the samples have a complete layered structure. Additionally, there are little differences in peak positions of (003) and (104) for the two samples, and their high values of $I_{(003)}/I_{(104)}$ peak ratios confirm that both the short and long rods have a great level of cation arrangement between Li^+ and Ni^{2+}.

Fig. 1e and f show the nitrogen adsorption–desorption isotherms of the short and long rods. It can be seen that both of the samples have a H1 type absorption-desorption behavior, indicating the existence of the porous structure in the rods. Specially, the BET specific surface area of the short rods (6.674 $m^2\ g^{-1}$) is slight bigger than that of the long rods (6.068 $m^2\ g^{-1}$). Additionally, the pore-size distribution plots show that both of the samples have a mesoporous structure.

The compositions of the short and long rods were measured by ICP. The data of Li/Mn/Ni/Co molar ratios are listed in Table 2. The results show that the compositions of the short and long rods are $Li_{1.210}Mn_{0.537}Ni_{0.126}Co_{0.127}O_2$ and $Li_{1.208}Mn_{0.536}Ni_{0.131}Co_{0.125}O_2$, respectively, which are approximately consistent with the $Li_{1.2}Mn_{0.54}Ni_{0.13}Co_{0.13}O_2$ stoichiometry.

The SEM images in Fig. 2a–c show the metal oxalate precursor prepared with $NH_3\cdot H_2O$ has a one-dimensional rod-like morphology. After the post-calcination treatment, the one-dimensional morphology of the metal oxalate precursor is inherited as shown in Fig. 2d. The low-magnification image in Fig. 2e displays that the lithium-rich material is composed of the short rods with about 2 μm length, around 300 nm thickness, and a good dispersed state. The high-magnification image in Fig. 2f presents that the short rods comprise many interconnected nano-sized particles, and possess a porous framework.

TEM characterization was carried out to obtain the structural insight of the short rods. The TEM images in Fig. 3a and b display that the nanoparticles link together to form the short rods with homogeneous structural integrity. The size of the nanoparticles is ~90 nm as shown in Fig. 3c, agreeing well with the results of the SEM observations. TEM image in Fig. 3d presents the network constructed by the nanoparticles. The high-resolution TEM image performed at the edge of the nanoparticle (Fig. 3d) clearly shows the parallel lattice fringes in Fig. 3e. The lattice fringe spacing is ~0.47 nm, corresponding to

Table 2 Li/Mn/Ni/Co molar ratios of the samples based on ICP-OES analysis

Sample	Li/Mn/Ni/Co molar ratio
The short rods	1.210/0.537/0.126/0.127
The long rods	1.208/0.536/0.131/0.125

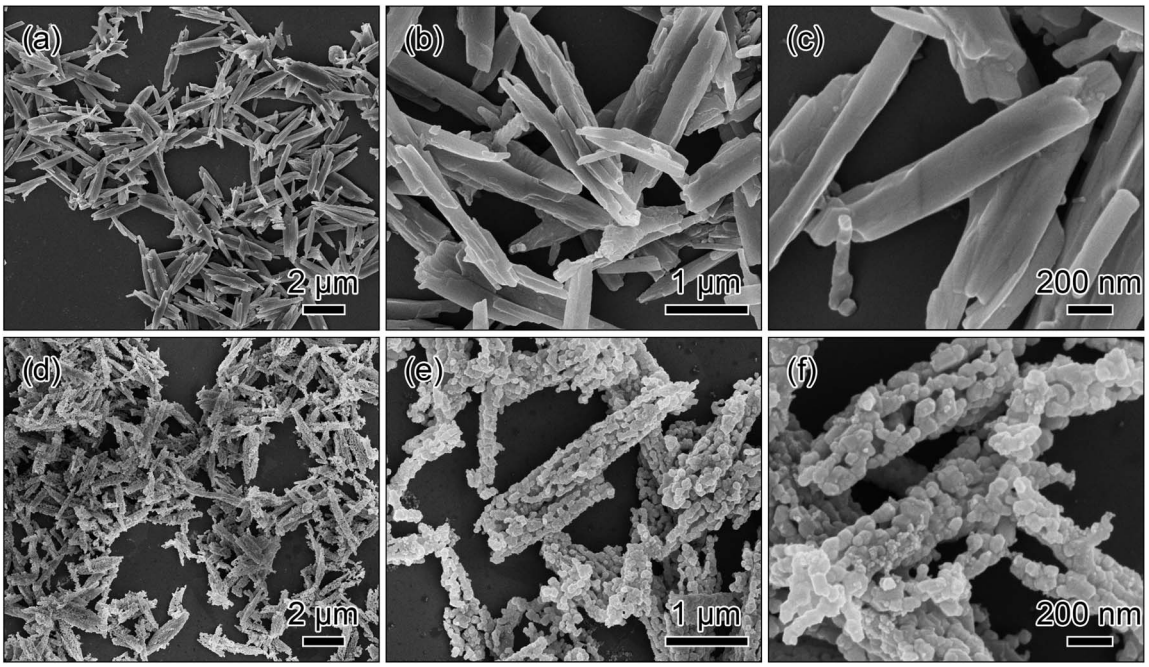

Fig. 2 SEM images of the metal oxalate precursor prepared *via* a co-precipitation method with the addition of $NH_3 \cdot H_2O$ (a–c) and the short rods obtained by a post-calcination treatment in air (d–f).

(003) plane of the rhombohedral $LiMO_2$ phase (space group $R\bar{3}m$) and (001) facet of the monoclinic Li_2MnO_3 phase (space group $C2/m$), indicating the high-quality and single-crystalline nature of the lithium-rich material.[23] In Fig. 3f, the selected area electron diffraction (SAED) pattern is taken from the zone axis along $[001]_{rhombohedral}$ and $[103]_{monoclinic}$ direction, suggesting the coexistence of $R\bar{3}m$ and $C2/m$ phases. The marked hexagon can be considered as the superposition of the $R\bar{3}m$ structure and the $C2/m$ structure rotated 120° around [103] direction, which is consent well with the overall hexagonal symmetry of lithium-rich layered materials.[24,25]

The added $NH_3 \cdot H_2O$ in the co-precipitation reaction is an important factor to fabricate the metal oxalate precursor. Here, the comparative experiment was conducted to clarify the role of $NH_3 \cdot H_2O$ in the co-precipitation reaction. For the comparative experiment, all the synthetic conditions were kept the same

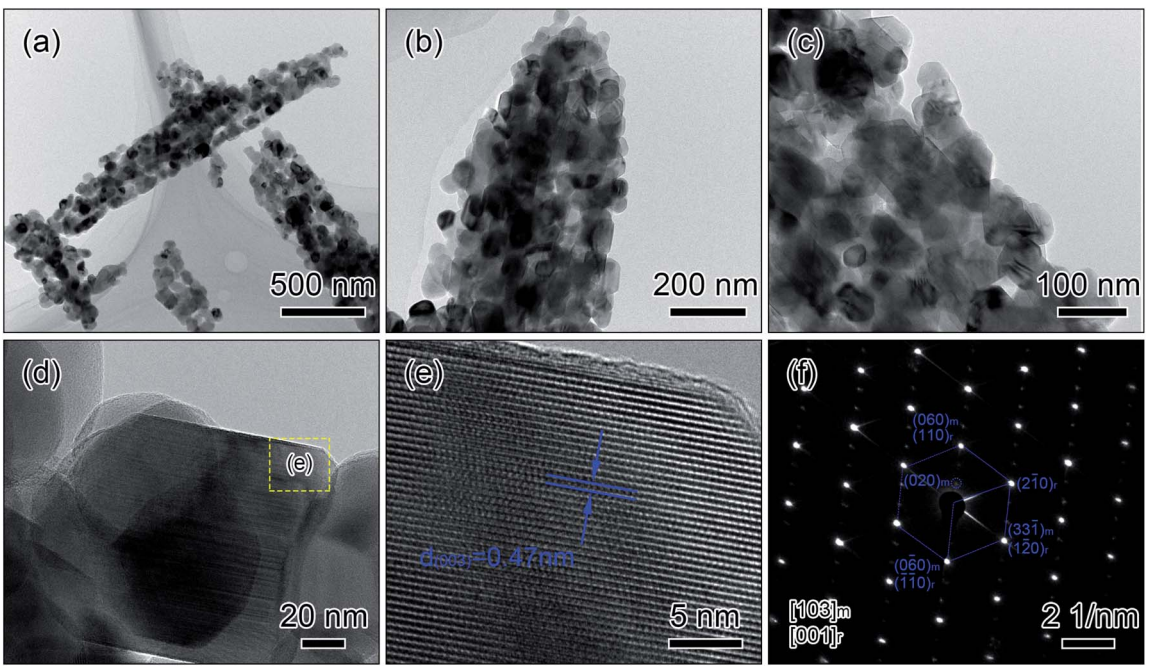

Fig. 3 TEM images at different magnifications (a–d), HRTEM image of the dashed region in (d) (e) and SAED pattern taken from the zone axis along $[001]_{rhombohedral}$ and $[103]_{monoclinic}$ direction (f) of the short rods.

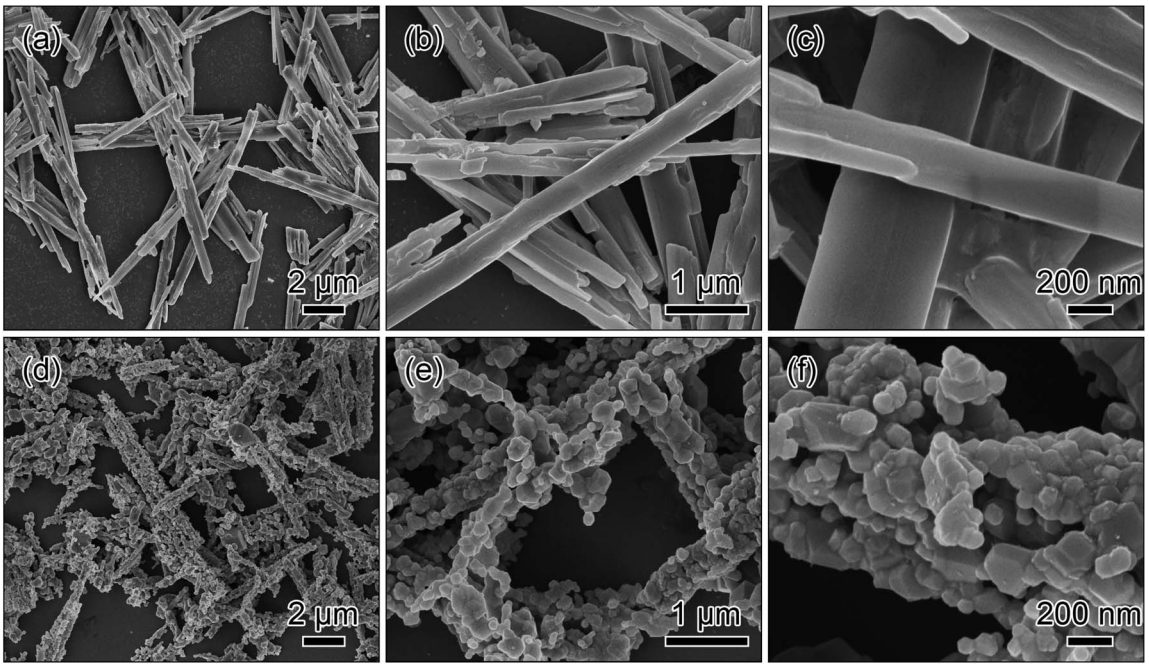

Fig. 4 SEM images of the metal oxalate precursor prepared *via* a co-precipitation method without the addition of $NH_3 \cdot H_2O$ (a–c) and the long rods obtained by a post-calcination treatment in air (d–f).

except without $NH_3 \cdot H_2O$. The SEM images in Fig. 4a–c show that the as-synthesized precursor is composed of the long rods with the length of 4–10 μm and the thickness of ~600 nm. After the calcination process, the morphology of the precursor is almost retained as shown in Fig. 4d. The magnified SEM images in Fig. 4e and f display that the long rods have a relatively broad particle size distribution.

Obviously, the results of the comparative experiment suggest that the addition of $NH_3 \cdot H_2O$ in the co-precipitation reaction plays a significant role in size-control of the metal oxalate precursors. Furthermore, the rods with a short length can offer an efficient electrolyte contact, a short Li^+ diffusion path and a stabilized matrix, which are expected to exhibit superior electrochemical performance.[26,27]

3.2. Size- and morphology-control mechanism of the rods

The above results reveal that the co-precipitation reaction with $NH_3 \cdot H_2O$ is favorable for the formation of the short rods, while the long rods are obtained by the reaction without $NH_3 \cdot H_2O$. Consequently, the size of the metal oxalate precursors with the one-dimensional morphology can be mainly determined by simply adding $NH_3 \cdot H_2O$ in the co-precipitation reaction. In general, the size of crystals can be related to their nucleation and growth kinetics mainly controlled by the factors such as the pH value, oversaturation and additives.[14,28] For the synthesis of the short rods, the extra ammonium hydroxide is added into the solution. As a result, a high pH value of the reaction medium may attribute to a high nucleation rate of the oxalate crystals.[29,30] On the other hand, ammonia and the dissolved Mn^{2+}, Ni^{2+} as well as Co^{2+} ions can be available for the formation of $[Mn–Ni–Co–(NH_3)_6]^{2+}$ complexes according to the following reaction (eqn (1)), which have been reported in previous works.[26,31] These $[Mn–Ni–Co–(NH_3)_6]^{2+}$ complexes in the solution can be behaved as the insoluble suspended matters, while other Mn^{2+}, Ni^{2+} and Co^{2+} ions in the solution may offer a circumstance with a proper oversaturation degree for the formation of the oxalates (eqn (2)). The proper oversaturation degree may lead to an appropriate growth rate of the oxalates. With the precipitation of the oxalates and the evaporation of ammonia, more Mn^{2+}, Ni^{2+} and Co^{2+} ions may be released from $[Mn–Ni–Co–(NH_3)_6]^{2+}$ complexes to the solution (eqn (3)) to keep the appropriate growth rate until all the complexes and lithium ions are consumed. The above discussion suggests that the high nucleation rate and appropriate growth speed of the oxalates originated from the adding $NH_3 \cdot H_2O$ may readily form the short rods under the co-precipitation condition. Conversely, the long rods may undergo a low nucleation rate as well as a fast growth rate in the co-precipitation condition.

$$Mn^{2+} + Ni^{2+} + Co^{2+} + 6NH_3 \rightarrow [Mn–Ni–Co–(NH_3)_6]^{2+} \quad (1)$$

$$1.2Li^+ + 0.54Mn^{2+} + 0.13Ni^{2+} + 0.13Co^{2+} + C_2O_4^{2-} + nH_2O \rightarrow Li_{1.2}Mn_{0.54}Ni_{0.13}Co_{0.13}C_2O_4 \cdot nH_2O \quad (2)$$

$$[Mn–Ni–Co–(NH_3)_6]^{2+} \rightarrow Mn^{2+} + Ni^{2+} + Co^{2+} + 6NH_3 \quad (3)$$

In addition, the two rods possess a one-dimensional morphology. Generally, the morphology of the precursors is highly dependent on the solvent of the reactions.[26,32] In this work, ethanol is used as the solvent in the co-precipitation reaction. Correspondingly, hydroxyl group of ethanol may preferentially adsorb on certain crystallite faces of the metal oxalate precursors.[14,33] Specifically, the growth of the capped

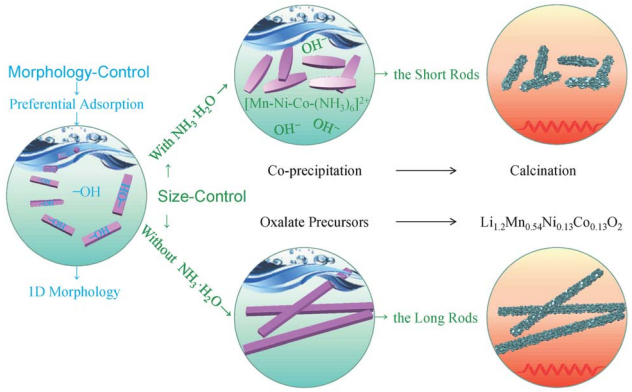

Fig. 5 Schematic illustration of size- and morphology-control mechanism of the rods prepared by the ethanol mediated co-precipitation with/without $NH_3 \cdot H_2O$ and the following calcination.

faces with hydroxyl group can be impeded, while the uncapped faces may mainly incline in one direction. As a result, the uncapped faces freely grow out, readily resulting in the one-dimensional morphology.

On the basis of the above discussions, the strategy to control of the size and morphology of the metal oxalate precursors is schematically illustrated in Fig. 5.

3.3. Electrochemical properties of the rods

The charge/discharge curves of 1st, 2nd, 10th, 50th and 100th cycles between 2.0 and 4.8 V at 0.1C for the two rods are shown in Fig. 6a and b. There are two plateaus from the initial charge curves of the two rods. The plateau (below 4.5 V) corresponds to the deintercalation of lithium ions from the layered structure combined with the oxidation reactions of Ni^{2+} to Ni^{4+} as well as Co^{3+} to Co^{4+}. The other plateau (above 4.5 V) relates to the oxygen extraction from the activation of Li_2MnO_3 phase.[34,35] For the following charge processes, the slopes of the curves increase and there is no obvious steady plateau (above 4.5 V), indicating that the activation process of Li_2MnO_3 phase during the initial charge is irreversible.[36] In detail, the short rods reach a discharge capacity of 286 mA h g^{-1} with a coulombic efficiency of 81% on the initial cycle, while the long rods deliver a discharge capacity of 280 mA h g^{-1} with a lower coulombic efficiency. In the subsequent cycles, high coulombic efficiencies over 95% can be achieved for both of the rods.

To further investigate the detail electrochemical behaviour during the cycles, cyclic voltammograms (CV) tests were conducted at a scan rate of 0.1 mV s^{-1} with a voltage range from 2.0 to 4.8 V. The CV plots of the two representative cycles for the two rods are shown in Fig. 6c. For the first cycle, both of the rods have two conspicuous oxidation peaks at about 4.0 V and 4.6 V. The former oxidation peak is associated to the deintercalation of lithium ions from the layered region, and the latter oxidation peak is related to oxygen loss from Li_2MnO_3 phase.[37] There are two broad reduction peaks at about 3.6 V and 3.3 V for the two rods. Correspondingly, the reduction reactions of Ni^{4+} to Ni^{2+} and Co^{4+} to Co^{3+} occur at about 3.6 V, and the reduction reaction of Mn^{4+} to Mn^{3+} occurs at about 3.3 V.[38] In the subsequent cycle, the oxidation peak of the two rods at 4.6 V disappears, and all the rest of peaks shift to lower voltages which correspond to the voltage decay of the discharge curves. In addition, a slow decay of voltage for the short rods can be observed by the comparison of the CV profiles, indicating that the short rods have a better reversibility.

Besides, the detailed contrasting cycle properties of the two rods at 0.1C are displayed in Fig. 6d. It can be obtained that the short and long rods maintain the discharge capacities of 243 and 213 mA h g^{-1} with the capacity retentions of 85 and 76% after 100 charge/discharge cycles, respectively. Obviously, the short rods show a better cycling stability.

Fig. 6e shows the discharge capacities of the two rods at high rates ranging from 0.5 to 10C. The discharge capacities of the short rods are 251 mA h g^{-1} at 0.5C, 227 mA h g^{-1} at 1C, 183 mA h g^{-1} at 5C and 152 mA h g^{-1} at 10C. When the rate reverts to 0.5C, the discharge capacity can still remain 248 mA h g^{-1}. In contrast, the long rods show inferior rate capabilities, exhibiting the discharge capacities of 248, 220, 163 and 117 mA h g^{-1} at 0.5, 1, 5 and 10C, respectively. And only a discharge capacity of 241 mA h g^{-1} is recovered back at 0.5C. Higher discharge capacities at various rates suggest better reaction kinetics.[39] These results indicate that the short rods exhibit the enhanced rate performance.

To further verify the improved reaction kinetics of the short rods, electrochemical impedance spectra (EIS) was performed before the cycle and after 100 cycles at 0.1C with the full discharging state. Nyquist plots of the two rods are shown in Fig. 6f–h. In Fig. 6f, the inset illustrates the corresponding equivalent circuit for fitting, where R_s, R_{ct}, CPE and Z_w correspond to the solution resistance, the charge transfer resistance, the capacitance and the Warburg resistance, respectively.[40,41] Based on the equivalent circuit fitting, R_s and R_{ct} of the short rods are 9.91 and 110.5 Ω, respectively, while R_s and R_{ct} of the long rods are 10.53 and 240.2 Ω. According to the slopes (σ) of the short (186 Ω cm^2 $s^{-1/2}$) and long (221 Ω cm^2 $s^{-1/2}$) rods in Fig. 6g and the Warburg equations,[33,35,37] Li^+ diffusion coefficients of the short (1.73×10^{-15} cm^2 s^{-1}) and long (1.22×10^{-15} cm^2 s^{-1}) rods can be calculated. The enhanced diffusion kinetics of Li^+ for the short rods could be contributed to their size advantages. Obviously, the short rods with a shorter length and smaller thickness can provide efficient electrolyte contact and fast Li^+ diffusion channels, which has been proved by many literatures.[11–14,42] Furthermore, the short rods exhibit a smaller change in the resistances after 100 cycles as shown in Fig. 6h, indicating that the short rods have a high structural stability during the cycle.

Based on the above electrochemical testing results, it is indicated that the short rods achieve the superior electrochemical performance in terms of the reversible capacity, rate capability as well as cycling stability in comparisons to the long rods. Particularly, the great dispersibility and homogeneous structural integration for the short rods which can be observed by the sem and tem images are advantageous for offering the appropriate contact area between the active material and the electrolyte, facilitating the efficient

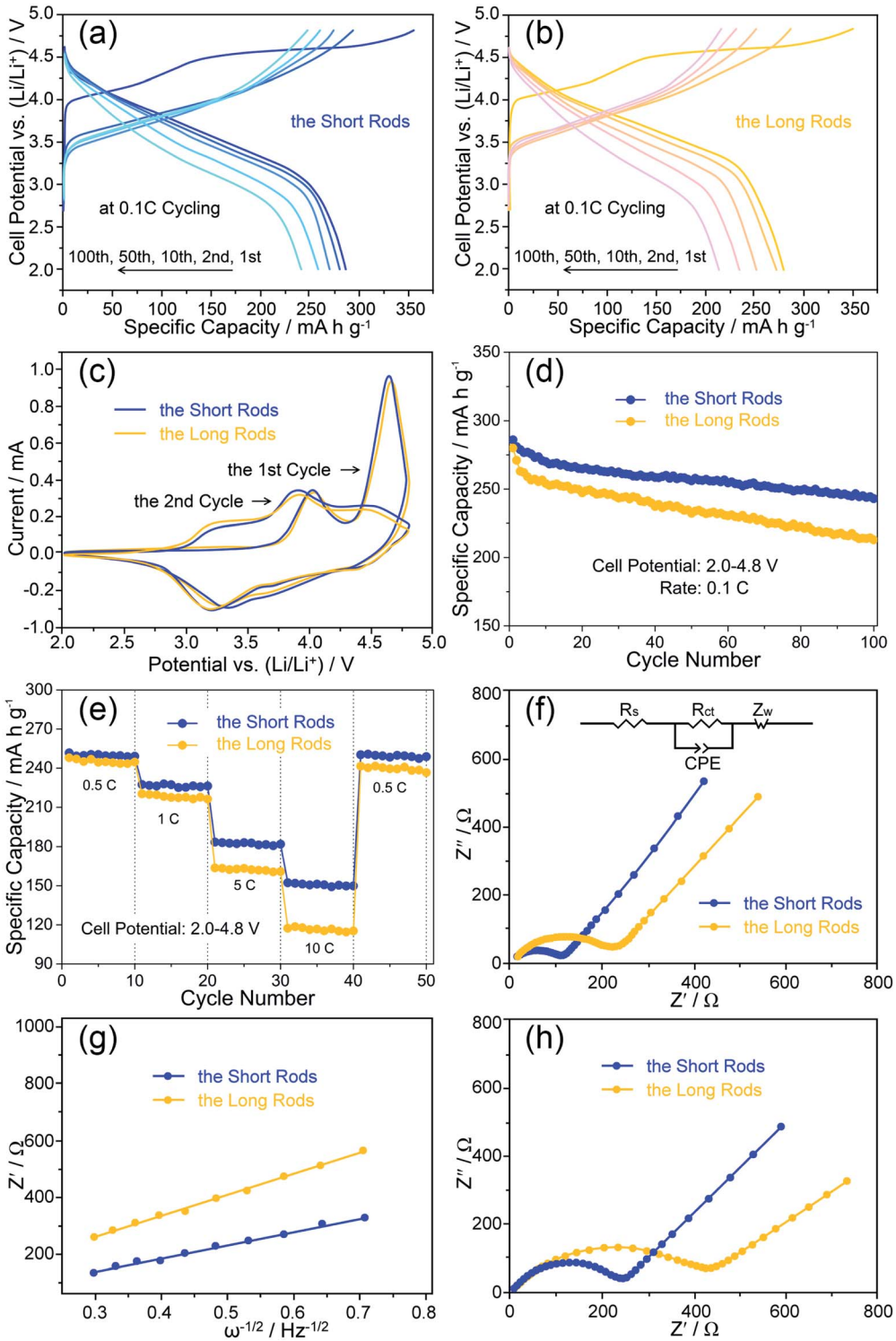

Fig. 6 Electrochemical performance of the short and long rods performed in the voltage range of 2.0–4.8 V *vs.* Li/Li^+: the charge/discharge curves at 0.1C (a and b), CV plots at a scan rate of 0.1 mV s^{-1} (c), cycling properties at 0.1C (d), rate capability at various rates (e), Nyquist plots (the inset is the equivalent circuit) obtained before the cycle (f), the relationship between Z' and $\omega^{-1/2}$ at low frequency region (g), and after 100 cycles (h) at 0.1C with the full discharging state.

electrolyte infiltration into the internal regions of the rods, and alleviating the mechanical strain associated with the volume changes during the repeated insertion/extraction of lithium ions. Consequently, the size advantages of good dispersed state and homogeneous structural integrity for the short rods afford the overall achievements of their superior electrochemical properties.

4. Conclusions

In summary, the $Li_{1.2}Mn_{0.54}Ni_{0.13}Co_{0.13}O_2$ rods with controllable sizes were fabricated by a facile co-precipitation method followed by a post-calcination treatment. It was demonstrated that the size of the metal oxalate precursors could be controlled by the adding $NH_3 \cdot H_2O$ in the co-precipitation reaction. The electrochemical properties of the as-obtained $Li_{1.2}Mn_{0.54}Ni_{0.13}Co_{0.13}O_2$ rods were influenced by their sizes. Particularly, the short rods exhibited a high capacity of 286 mA h g^{-1} at 0.1C and had a capacity retention of 85% after 100 cycles. The enhanced electrochemical performance of the short rods could be contributed to their size advantages, providing efficient electrolyte contact, fast Li^+ diffusion channels and good structure stability.

Conflicts of interest

There are no conflicts to declare.

Acknowledgements

This work was financially supported by the National Natural Science Foundation of China (grant numbers 51762022), the Natural Science Foundation of Jiangxi Province (grant number 20171BAB206026 and 20192ACBL20029 and 20202BABL204031), and the Science & Technology Research Program of Jiangxi Provincial Education Department (grant number GJJ190539 and GJJ201013).

Notes and references

1 J. B. Goodenough and K. S. Park, *J. Am. Chem. Soc.*, 2013, **135**, 1167–1176.
2 Y. Lu, Q. Zhang and J. Chen, *Sci. China: Chem.*, 2019, **62**, 533–548.
3 A. Manthiram, *Nat. Commun.*, 2020, **11**, 1550.
4 W. Li, B. Song and A. Manthiram, *Chem. Soc. Rev.*, 2017, **46**, 3006–3059.
5 S. H. Kang, Y. K. Sun and K. Amine, *Electrochem. Solid-State Lett.*, 2003, **6**, A183.
6 M. M. Thackeray, C. S. Johnson, J. T. Vaughey, N. Li and S. A. Hackney, *J. Mater. Chem.*, 2005, **15**, 2257–2267.
7 P. Rozier and J. M. Tarascon, *J. Electrochem. Soc.*, 2015, **162**, A2490–A2499.
8 S. Hy, H. Liu, M. Zhang, D. Qian, B. J. Hwang and Y. S. Meng, *Energy Environ. Sci.*, 2016, **9**, 1931–1954.
9 H. Yu and H. Zhou, *J. Phys. Chem. Lett.*, 2013, **4**, 1268–1280.
10 K. Zhang, B. Li, Y. Zuo, J. Song, H. Shang, F. Ning and D. Xia, *Electrochem. Energy Rev.*, 2019, **2**, 606–623.
11 Q. Wei, F. Xiong, S. Tan, L. Huang, E. H. Lan, B. Dunn and L. Mai, *Adv. Mater.*, 2017, **29**, 1602300.
12 B. Deng, Y. Chen, P. Wu, J. Han, Y. Li, H. Zheng, Q. Xie, L. Wang and D. L. Peng, *J. Power Sources*, 2019, **418**, 122–129.
13 H. He, L. Zan, J. Liu and Y. Zhang, *Electrochim. Acta*, 2020, **333**, 135558.
14 G. Ma, S. Li, W. Zhang, Z. Yang, S. Liu, X. Fan, F. Chen, Y. Tian, W. Zhang, S. Yang and M. Li, *Angew. Chem., Int. Ed.*, 2016, **55**, 3667–3671.
15 G. Wang, L. Yi, R. Yu, X. Wang, Y. Wang, Z. Liu, B. Wu, M. Liu, X. Zhang, X. Yang, X. Xiong and M. Liu, *ACS Appl. Mater. Interfaces*, 2017, **9**, 25358–25368.
16 S. Kong, Y. Gong, P. Liu, Y. Xiao, F. Qi and X. Z. Zhao, *Ceram. Int.*, 2019, **45**, 13011–13018.
17 M. M. Thackeray, S. H. Kang, C. S. Johnson, J. T. Vaughey and S. A. Hackney, *Electrochem. Commun.*, 2006, **8**, 1531–1538.
18 K. A. Jarvis, Z. Deng, L. F. Allard, A. Manthiram and P. J. Ferreira, *Chem. Mater.*, 2011, **23**, 3614–3621.
19 C. S. Johnson, N. Li, C. Lefief, J. T. Vaughey and M. M. Thackeray, *Chem. Mater.*, 2008, **20**, 6095–6106.
20 J. M. Zheng, X. B. Wu and Y. Yang, *Electrochim. Acta*, 2011, **56**, 3071–3078.
21 Y. Wu and A. Manthiram, *J. Power Sources*, 2008, **183**, 749–754.
22 H. Z. Zhang, Q. Q. Qiao, G. R. Li, S. H. Ye and X. P. Gao, *J. Mater. Chem.*, 2012, **22**, 13104–13109.
23 G. Z. Wei, X. Lu, F. S. Ke, L. Huang, J. T. Li, Z. X. Wang, Z. Y. Zhou and S. G. Sun, *Adv. Mater.*, 2010, **22**, 4364–4367.
24 H. Li, X. Wei, P. Yang, Y. Ren, S. Wang, Y. Xing and S. Zhang, *Electrochim. Acta*, 2018, **261**, 86–95.
25 M. Vivekanantha, C. Senthil, T. Kesavan, T. Partheeban, M. Navaneethan, B. Senthilkumar, P. Barpanda and M. Sasidharan, *Electrochim. Acta*, 2019, **317**, 398–407.
26 F. Fu, Y. Yao, H. Wang, G. L. Xu, K. Amine, S. G. Sun and M. Shao, *Nano Energy*, 2017, **35**, 370–378.
27 D. Chen, Q. Yu, X. Xiang, M. Chen, Z. Chen, S. Song, L. Xiong, Y. Liao, L. Xing and W. Li, *Electrochim. Acta*, 2015, **154**, 83–93.
28 X. Pan, Z. Gao, L. Liu, F. Xiao, F. Xiao, S. Xie and R. Yi, *J. Alloys Compd.*, 2019, **783**, 468–477.
29 N. Rapulenyane, E. Ferg and H. Luo, *J. Alloys Compd.*, 2018, **762**, 272–281.
30 L. Huang, L. Liu, H. Wu, Y. Wang, H. Liu and Y. Zhang, *J. Alloys Compd.*, 2019, **775**, 921–930.
31 X. Li, G. L. Xu, F. Fu, Z. Lin, Q. Wang, L. Huang, J. T. Li and S. G. Sun, *Electrochim. Acta*, 2013, **96**, 134–140.
32 H. Li, Y. Ren, P. Yang, Z. Jian, W. Wang, Y. Xing and S. Zhang, *Electrochim. Acta*, 2019, **297**, 406–416.
33 J. Zeng, Y. Cui, D. Qu, Q. Zhang, J. Wu, X. Zhu, Z. Li and X. Zhang, *ACS Appl. Mater. Interfaces*, 2016, **8**, 26082–26090.
34 S. Hy, F. Felix, J. Rick, W. N. Su and B. J. Hwang, *J. Am. Chem. Soc.*, 2014, **136**, 999–1007.
35 Y. Ma, P. Liu, Q. Xie, G. Zhang, H. Zheng, Y. Cai, Z. Li, L. Wang, Z. Z. Zhu, L. Mai and D. L. Peng, *Nano Energy*, 2019, **59**, 184–196.
36 A. R. Armstrong, M. Holzapfel, P. Novák, C. S. Johnson, S. H. Kang, M. M. Thackeray and P. G. Bruce, *J. Am. Chem. Soc.*, 2006, **128**, 8694–8698.
37 Y. Zhang, T. Zhu, L. Lin, M. Yuan, H. Li, G. Sun and S. Ma, *J. Nanopart. Res.*, 2017, **19**, 373.
38 M. Sathiya, G. Rousse, K. Ramesha, C. P. Laisa, H. Vezin, M. T. Sougrati, M. L. Doublet, D. Foix, D. Gonbeau,

W. Walker, A. S. Prakash, M. Ben Hassine, L. Dupont and J. M. Tarascon, *Nat. Mater.*, 2013, **12**, 827–835.
39 L. Zhang, N. Li, B. Wu, H. Xu, L. Wang, X. Q. Yang and F. Wu, *Nano Lett.*, 2015, **15**, 656–661.
40 D. Andre, M. Meiler, K. Steiner, C. Wimmer, T. Soczka-Guth and D. U. Sauer, *J. Power Sources*, 2011, **196**, 5334–5341.
41 T. Liu, S. X. Zhao, L. L. Gou, X. Wu and C. W. Nan, *Rare Met.*, 2019, **38**, 189–198.
42 C. C. Xu, Y. Wang, L. Li, Y. J. Wang, L. F. Jiao and H. T. Yuan, *Rare Met.*, 2019, **38**, 29–34.